13. D. C. Chu and G. E. Karniadakis, *J. Fluid Mech.* **250**, 1 (1993).
14. L. Sirovich and S. Karlsson, *Nature* **388**, 753 (1997).
15. W. J. Jung, N. Mangiavacchi, R. Akhavan, *Phys. Fluids* **4**, 1605 (1992).
16. W. Schoppa and F. Hussain, in *Proceedings on Self-Sustaining Mechanics of Wall Turbulence*, R. Panton, Ed. (Computational Mechanics Publications, Billerica, MA, 1997), pp. 385–422.
17. F. Wallefe, *Phys. Fluids* **9**, 883 (1997).
18. C.-M. Ho and Y.-C. Tai, *J. Fluids Eng.* **118**, 437 (1996).
19. C. D. Near, *Proc. SPIE* **2717**, 246 (1996).
20. O. K. Rediniotis, D. C. Lagoudas, L. N. Wilson, *AIAA Paper No. AIAA 2000-0522* (American Institute of Aeronautics and Astronautics, Reston, VA, 2000).
21. D. Nosenchuck and G. L. Brown, in *International Conference on Near-Wall Turbulent Flows*, C. G. Speziale and B. E. Launder, Eds. (Elsevier, Amsterdam, 1993), pp. 689–698.
22. D. Nosenchuck, in *Proceedings of ASME Fluid Engineering Meeting* (American Society of Mechanical Engineers, New York, 1996), pp. 1–9.
23. D. Nosenchuck, private communication; R. Philips, private communication.
24. C. H. Crawford and G. E. Karniadakis, *Phys. Fluids* **9**, 788 (1997).
25. C. Henoch and J. Stace, *Phys. Fluids* **7**, 1371 (1995).
26. This work was supported by the Defense Advanced Research Projects Agency and the Naval Undersea Warfare Center and partially (work on numerical methods) by the Office of Naval Research. We are grateful to R. Philips and D. Nosenchuck for making unpublished experimental results available to us. The computations were performed on the O2000 at the National Center for Supercomputing Applications and on the SP at Maui High Performance Computing Center. We would like to dedicate this paper to the memory of L. Krall, with whom we had very valuable discussions on turbulent drag reduction during the course of this project.

24 January 2000; accepted 14 March 2000

The Spin Excitation Spectrum in Superconducting $YBa_2Cu_3O_{6.85}$

P. Bourges,[1*] Y. Sidis,[1] H. F. Fong,[2] L. P. Regnault,[3] J. Bossy,[4] A. Ivanov,[5] B. Keimer[2,6]

A comprehensive inelastic neutron scattering study of magnetic excitations in the near optimally doped high-temperature superconductor $YBa_2Cu_3O_{6.85}$ is presented. The spin correlations in the normal state are commensurate with the crystal lattice, and the intensity is peaked around the wave vector characterizing the antiferromagnetic state of the insulating precursor, $YBa_2Cu_3O_6$. Profound modifications of the spin excitation spectrum appear abruptly below the superconducting transition temperature T_c, where a commensurate resonant mode and a set of weaker incommensurate peaks develop. The data are consistent with models that are based on an underlying two-dimensional Fermi surface, predicting a continuous, downward dispersion relation connecting the resonant mode and the incommensurate excitations. The magnetic incommensurability in the $YBa_2Cu_3O_{6+x}$ system is thus not simply related to that of another high-temperature superconductor, $La_{2-x}Sr_xCuO_4$, where incommensurate peaks persist well above T_c. The temperature-dependent incommensurability is difficult to reconcile with interpretations based on charge stripe formation in $YBa_2Cu_3O_{6+x}$ near optimum doping.

Electronic conduction in the high-temperature superconductor cuprate takes place predominantly in CuO_2 layers. Most theories therefore regard the electronic state that forms the basis of high-temperature superconductivity as an essentially two-dimensional (2D) strongly correlated metal. The CuO_2 sheets in one family of copper oxides ($La_{2-x}Sr_xCuO_4$) have, however, been shown to be unstable against the formation of 1D "charge stripes" (*1*), even near doping levels where the superconducting transition temperature T_c is maximum. This observation has boosted models in which the underlying electronic instability is 1D and the formation of (static or fluctuating) stripes is an essential precondition for high-temperature superconductivity [see, e.g., (*2*)]. However, $La_{2-x}Sr_xCuO_4$ has some low-energy phonon modes conducive to stripe formation that are not generic to the high-T_c compounds, and the maximum T_c in this system is anomalously low. It is therefore important to test whether stripe-based scenarios are viable in other cuprates with higher T_c, where this lattice dynamical peculiarity is not present.

The most salient signature of charge stripes is an associated (static or dynamic) spin density modulation that can be detected by neutron scattering. In $La_{2-x}Sr_xCuO_4$, this modulation manifests itself as four well-defined incommensurate peaks at wave vectors $\mathbf{Q}_\delta = (\pi(1 \pm \delta), \pi)$ and $(\pi, \pi(1 \pm \delta))$ (in square lattice notation with unit lattice constant; δ is the incommensurability parameter) in the magnetic spectrum (*3–6*), which are interpreted as arising from two 1D domains. Neutron scattering experiments on the $YBa_2Cu_3O_{6+x}$ system have, however, revealed excitations that are peaked at $\mathbf{Q}_{AF} = (\pi, \pi)$ (*7–13*), the ordering wave vector of the 2D antiferromagnetic state observed when the doping level is reduced to zero. In particular, the commensurate "resonance peak" at (π, π) that dominates the spectrum in the superconducting state (*9–15*) is difficult to reconcile with scenarios based on fluctuating 1D domains incommensurate with the host lattice. Recently, an incommensurate pattern with a fourfold symmetry reminiscent of $La_{2-x}Sr_xCuO_4$ has also been discovered in some constant-energy cuts of the magnetic spectrum of underdoped $YBa_2Cu_3O_{6.6}$ (*16–18*), which was taken as experimental support for stripe-based scenarios of superconductivity. We report a neutron scattering study of near optimally doped $YBa_2Cu_3O_{6.85}$ (T_c = 89 K), demonstrating that (unlike in $La_{2-x}Sr_xCuO_4$) the incommensurate pattern appears only below T_c. Magnetic excitations in the normal state are commensurate and centered at $\mathbf{Q} = (\pi, \pi)$. Our data are consistent with 2D Fermi liquid–like theories (not invoking stripes) (*19–23*) and especially that which predicts a continuous, downward dispersion of the magnetic resonance peak (*20*).

The experiments were performed on a large twinned single crystal (mass of ~9.5 g) grown using the top seed melt texturing method (*24*). The sample was subsequently annealed in oxygen and displays a sharp superconducting transition (T_c) at 89 K measured by a neutron depolarization technique that is sensitive to the entire bulk (*24*). Experiments were carried out on two triple-axis spectrometers: IN8 at the Institut Laue-Langevin, Grenoble (France), and 2T at the Laboratoire Léon Brillouin, Saclay (France) (*25*). Two different scattering geometries were used on both spectrometers. On IN8, the (130) and (001) reciprocal directions were within the horizontal scattering plane. [We quote the wave vector $\mathbf{Q} = (H, K, L)$ in units of the tetragonal reciprocal lattice vectors $a^* = 2\pi/a = 2\pi/b = 1.63$ Å^{-1} and $c^* = 2\pi/c = 0.53$ Å^{-1} (a, b, and c are lattice parameters).] On 2T, an unconventional scattering geometry has been employed with the (100) and (011) reciprocal directions spanning the scattering plane. In both scattering geometries, in-plane wave vectors equivalent to (π, π) can be reached, with an out-of-plane wave vector component close to the maximum of the structure factor of low-energy excitations (*24*). In addition, wave vectors of the form $\mathbf{Q} = (H, K, 1.7)$ around the

[1]Laboratoire Léon Brillouin, Commissariat à l'Energie Atomique–CNRS, CE Saclay, 91191 Gif sur Yvette, France. [2]Department of Physics, Princeton University, Princeton, NJ 08544, USA. [3]Département de Recherche Fondamentale sur la Matière Condensée, Commissariat à l'Energie Atomique Grenoble, 38054 Grenoble cedex 9, France. [4]CNRS–Centre de Recherches sur les Très Basses Températures, BP 166, 38042 Grenoble cedex 9, France. [5]Institut Laue-Langevin, 156X, 38042 Grenoble cedex 9, France. [6]Max-Planck-Institut für Festkörperforschung, 70569 Stuttgart, Germany.

*To whom correspondence should be addressed. E-mail: bourges@bali.saclay.cea.fr

antiferromagnetic wave vector were accessible on 2T by controlling the tilt angle, allowing for 2D mapping of the neutron intensity in the tetragonal basal momentum space and for a fixed energy transfer.

The magnetic resonance peak was observed at an energy E_r = 41 meV and $\mathbf{Q} = \mathbf{Q}_{AF}$ in our sample (*24*) in agreement with previous reports for similar oxygen content (*7, 12*). Here we present data obtained at energies below the resonance where the magnetic signal is substantially weaker. Using established procedures, we used the temperature dependence of the magnetic intensity (which strongly decreases upon heating) to separate it from the phonon scattering that gradually increases with increasing temperature (Fig. 1A). Figure 1, B through D, shows constant-energy scans at E = 35 meV performed along the (130) direction (arrow in the inset of Fig. 1B). The phonon contribution has been subtracted for clarity. At low temperature, deep in the superconducting state, the magnetic scattering exhibits a double-peak structure along (H, 3H, 0). At 70 K, the intensity is still peaked at incommensurate wave vectors, but the discommensuration is slightly reduced. A single broad feature peaked at H = 0.5 was observed at 100 K in the normal state.

We performed a comprehensive set of measurements to chart out in detail the spectral rearrangement indicated in Fig. 1. As an example, typical constant-energy scans were taken at low temperature along the H direction with K = 1.5 (Fig. 2A). The magnetic intensity is maximum at incommensurate wave vectors displaced from (0.5, 1.5) along H, and the incommensurability in this direction depends continuously on energy and forms a dispersing branch that closes at E_r. Accordingly, the maximum of the spin susceptibility at a wave vector sufficiently far from (π, π) is shifted to a lower energy than the resonant peak energy. The profile shapes are influenced by the instrumental resolution, and a deconvolution is required to accurately extract the peak positions. We found that a good global fit to the peak positions in both scattering geometries could be obtained by a convolution of the spectrometer resolution with the dispersion relation $E = [E_r^2 - (\alpha q)^2]^{1/2}$ with α = (125 ± 15) meV·Å (*26*). This downward dispersion (Fig. 2B) is shown along with the fitted peak positions. A neutron intensity map in the (H, K) reciprocal lattice plane measured at E = 35 meV and T = 12 K (not shown here) indicates that the intensity is not uniform along the dispersion surface. As in more underdoped samples (*17, 18*), the intensity pattern has fourfold symmetry, with maxima shown as full squares in the inset of Fig. 1B. Although the data have not been analyzed in this manner, the overall momentum dependence of the spin susceptibility reported in Fig. 3 below T_c is consistent with that reported in (*16*) and (*18*) as well as with that in (*10*) and (*15*) where the incommensurability was not resolved.

Similar scans were repeated in the normal state (Fig. 3B), where the data thus far reported are inconclusive about the incommensurability. For all energies reported in Fig. 2, the normal-state response can be systematically fitted by a single broad line (as shown at E = 35 meV in Fig. 1D). Figure 3 shows that the momentum width at T = 100 K is energy independent up to 45 meV, where the peaks begin to broaden (*27*). The momentum width (hereafter q width) at low energy, Δ_q = 0.21 Å^{-1} (half width at half maximum) after deconvolution, agrees with previous reports for a similar oxygen content (*15, 28*). Below T_c, the spin dynamics exhibit a more complex momentum dependence (Fig. 3A). Although the momentum shape at energies above 45 meV is largely unaffected by superconductivity, there is a large increase in intensity and narrowing of the q width at E_r = 41 meV, which is accompanied by a much weaker incommensurate response in a narrow energy range below E_r. Finally, the intensity is strongly reduced below 30 meV, which could result from the opening of a "spin gap" below T_c, as suggested by previous measurements (*7, 12*).

The incommensurate response thus appears to be intimately linked to the occurrence of the resonance peak below T_c (*7, 9–15, 24, 29*). To complete this picture, we now describe an accurate determination of the onset temperature of the incommensurate response and compare it to that of the resonance peak (*8, 10–15*). The temperature dependence of the resonance intensity is reproduced for the present sample (Fig. 4A), and the raw neutron intensity (say without the phonon background subtracted) at the incommensurate position $\mathbf{Q}$ = (0.4, 1.5, 1.7) and E = 35 meV is shown versus temperature (Fig. 4B). Processed data at E = 35 meV [phonons subtracted and converted to absolute units (*11, 24*)] are shown (Fig. 4C) as a series of wave vectors (open diamonds in Fig. 2B) spanning the locus of maximum intensity at low temperatures. All curves show a precipitous upturn at T_c, demonstrating that both the resonance peak and the incommensurability are induced by superconductivity. An indication of similar behavior had already been found in $YBa_2Cu_3O_{6.7}$ (T_c = 67 K) (*29*) so that this behavior seems to be generic to the $YBa_2Cu_3O_{6+x}$ superconductor.

Figure 4C is also revealing in another respect. Although all curves show the same sharp initial upturn below T_c, the imaginary part of the spin susceptibility χ'' ($\mathbf{Q}$, 35 meV) generally goes through a maximum at a temperature $T_m(\mathbf{Q})$ that increases as $\mathbf{Q} \rightarrow (\pi, \pi)$. A monotonic temperature dependence ($T_m \rightarrow 0$) like the one of the resonance peak is seen only for $\mathbf{Q}$ close to the low-temperature incommensurate wave vector determined above. However, the difference $\chi''(T_m) - \chi''(T_c)$ is identical within the errors for the three $\mathbf{Q}$ points away from (π, π). This dramatic behavior can be straightforwardly understood as a consequence of the temperature- and energy-dependent incommensurability already indicated above (Fig. 1 and

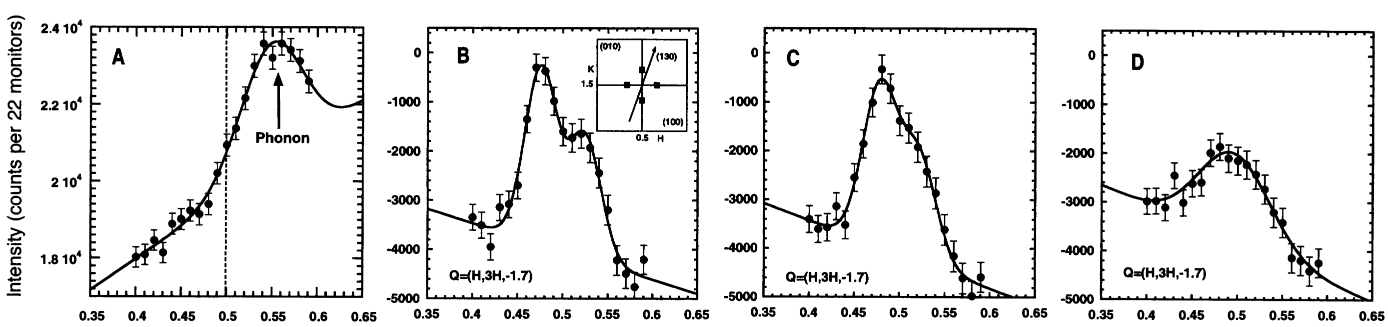

Fig. 1. (**A**) Raw (uncorrected) room-temperature scan, which exhibits a phonon peak around H = 0.57. (**B** through **D**) Neutron intensity (I) of constant-energy scans at E = 35 meV performed along the (130) direction, with the room-temperature scan subtracted as follows: in (B), I(11 K) – I(300 K); in (C), I(70 K) – I(300 K); and in (D), I(100 K) – I(300 K). The momentum resolution was 0.03 r.l.u. (= 0.15 Å^{-1}) along the (1, 3, 0) direction and 0.06 r.l.u. (= 0.3 Å^{-1}) along the vertical direction. The energy resolution was 5 meV. We cannot rule out a small antiferromagnetic intensity (about one-fourth that at 100 K) at room temperature. The scan in (A) displays none of the features of (B) through (D). The inset in (B) is a sketch of the reciprocal space around the antiferromagnetic wave vector. The squares represent the locus of maximum magnetic intensity in the superconducting state. The arrow represents the (130) direction of the scans. Error bars in (A) through (D) indicate statistical errors.

Figs. 2 and 3, respectively). The resonance peak, together with the dispersion, forms quickly upon cooling below T_c and then sweeps sequentially through the wave vectors monitored in Fig. 4C.

In $YBa_2Cu_3O_{6.85}$, the incommensurate response is part of a continuous dispersion below the resonance peak that is strongly renormalized upon approaching T_c and vanishes in the normal state. This is in stark contrast to the behavior reported for $La_{2-x}Sr_xCuO_4$ (*3–6*), where no change of the peak position occurs across the superconducting temperature (*3*). Only around room temperature does the incommensurate structure begin to disappear (*30*). Further, δ is energy independent in $La_{2-x}Sr_xCuO_4$ but depends strongly on doping over a wide range of the phase diagram (*6*). Because of the energy dependence of δ discussed above and the small number of samples investigated thus far, information about its doping dependence in $YBa_2Cu_3O_{6+x}$ is still incomplete. However, at $E = 35$ meV ($= E_r - 6$ meV), the discommensuration that we found in $YBa_2Cu_3O_{6.85}$, $\delta = 0.10$ reduced lattice units (r.l.u.) $\equiv 0.16$ Å^{-1}, is equal to that reported in $YBa_2Cu_3O_{6.6}$ (*17*) at $E = 24.5$ meV ($= E_r' - 9.5$ meV with $E_r' = 34$ meV) within the experimental error. Finally, the incommensurate fluctuations are only observed in a narrow energy range for fixed doping and are further substantially weakened in fully oxidized $YBa_2Cu_3O_7$ (*9, 10, 12*).

In the light of these observations, the analogy between the incommensurate spin excitations in $La_{2-x}Sr_xCuO_4$ and $YBa_2Cu_3O_{6+x}$ should not be overstated. Specifically, the interpretation in terms of stripe-domain fluctuations with a well-defined, doping-dependent average periodicity, which is compelling and well-documented in $La_{2-x}Sr_xCuO_4$, seems untenable in $YBa_2Cu_3O_{6+x}$ near optimal doping. Our data indicate that the incommensurate excitations are continuously connected to the commensurate resonance peak by a dispersion relation with a negative curvature (Fig. 1B). The temperature dependence of Fig. 4 strongly supports a common origin of both phenomena. Some aspects of the behavior we observed have, in fact, been anticipated in the framework of microscopic models, where the resonance peak is interpreted as a collective mode pulled below the gapped particle-hole spin-flip continuum (*19–21*). In particular, a downward dispersion has been predicted to arise naturally as a result

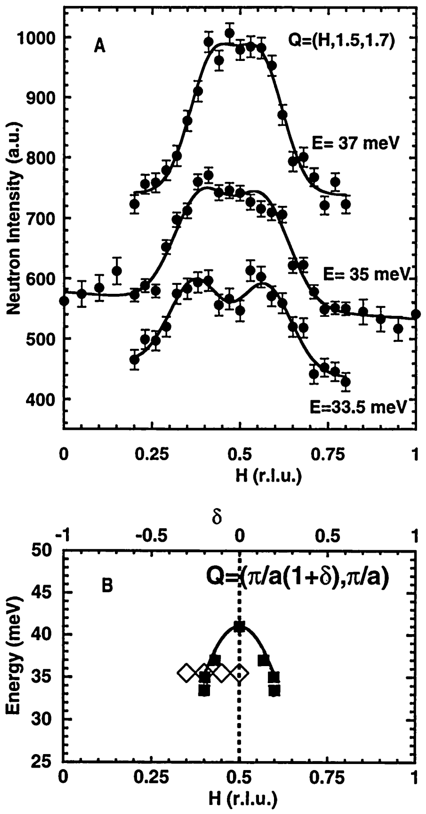

Fig. 2. (**A**) Constant-energy scans performed along the *H* direction. The scans are offset by 120 counts from each other. The momentum resolution (full width at half maximum) was 0.14 r.l.u. along *H* and 0.1 r.l.u. along *K*. The energy resolution was 4 meV. The lines are Gaussian displaced by $\pm\delta H$ from $\mathbf{Q}_{AF}$. The momentum transfer along c* was fixed to the maximum of the magnetic structure factor, $L = 1.7$. The phonon background measured at room temperature was subtracted from the data after proper correction for the Bose population factor (*15*). Error bars indicate statistical errors. (**B**) Dispersion of the incommensurate peaks observed in $YBCO_{6.85}$, deduced from (A) as described in the text. The square at $H = 0.5$ represents the resonance peak, $E_r = 41$ meV. The other squares at $0.5 \pm \Delta H$ come from the Gaussian fits shown in the upper panel. The open diamonds indicate the four wave vectors at $E = 35$ meV, where the temperature dependence has been studied (see Fig. 4).

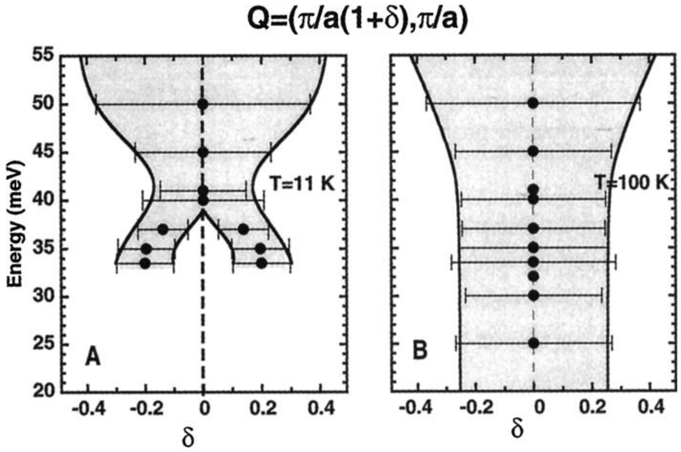

Fig. 3. Overall momentum dependence of the magnetic response in $YBCO_{6.85}$ obtained (**A**) in the superconducting state at $T = 11$ K and (**B**) in the normal state at $T = 100$ K. Error bars indicate the momentum width, Δ_q.

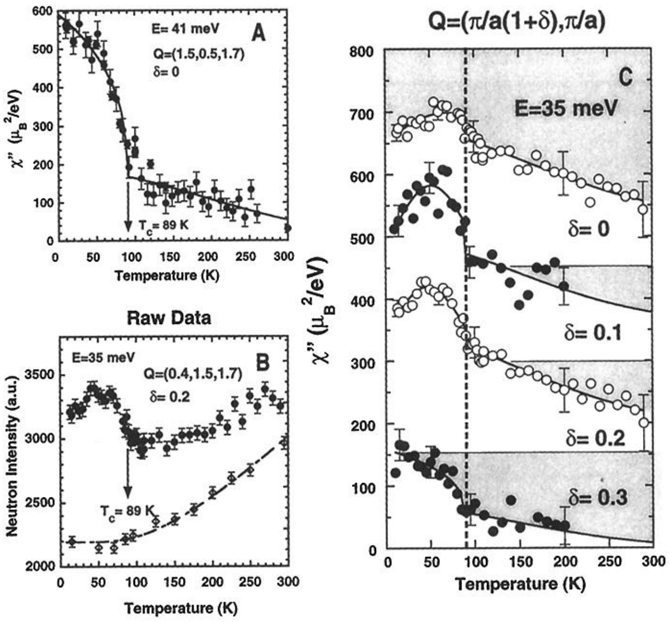

Fig. 4. (**A**) Temperature dependence of spin susceptibility in absolute units at the resonance energy $E = 41$ meV. μ_B, Bohr magneton. Error bars indicate statistical errors. (**B**) Temperature dependence of the neutron intensity at $E = 35$ meV and at the incommensurate wave vector $\mathbf{Q}_\delta = (1.5, 0.4, 1.7)$ (solid circles). The open diamonds represent the background, determined by constant-energy scans (equivalent to the one shown in Fig. 2A). Error bars indicate statistical errors. (**C**) Temperature dependence of spin susceptibility in absolute units at $E = 35$ meV for four momentum transfers along *a** (four open diamonds in Fig. 2B). The curves have been shifted by 150 μ_B^2/eV from one another. The susceptibility has been obtained by background subtraction and correction for the temperature factor $1/[1 - \exp(-E/k_BT)]$ (k_B, Boltzmann constant). A change at T_c is observed at all wave vectors. Error bars indicate statistical errors.

of a momentum-dependent pole in the spin susceptibility due to antiferromagnetic interactions (*20*). This picture also accounts for the rapidly diminishing intensity of the magnetic peaks away from (π, π), as collective modes commonly lose oscillator strength upon approaching the continuum. Models based on dynamical nesting induced by a modification of the band dispersions (*21–23*) may also be consistent with our data. The models favored by our experimental results on near optimally doped $YBa_2Cu_3O_{6+x}$ are based on an interplay between band dispersions, Coulomb interactions, and the *d*-wave gap function in a 2D correlated electronic state.

References and Notes

1. J. M. Tranquada *et al.*, *Nature* **375**, 561 (1995).
2. V. J. Emery and S. A. Kivelson, *Physica C* **209**, 597 (1993).
3. T. E. Mason *et al.*, *Phys. Rev. Lett.* **68**, 1414 (1992).
4. T. R. Thurston *et al.*, *Phys. Rev. B* **46**, 9128 (1992).
5. S. Petit *et al.*, *Physica B* **234–236**, 800 (1997).
6. K. Yamada *et al.*, *Phys. Rev. B* **57**, 6165 (1998).
7. J. Rossat-Mignod *et al.*, *Physica C* **185–189**, 86 (1991).
8. H. A. Mook *et al.*, *Phys. Rev. Lett.* **70**, 3490 (1993).
9. H. F. Fong *et al.*, *Phys. Rev. Lett.* **75**, 316 (1995).
10. P. Bourges, L. P. Regnault, Y. Sidis, C. Vettier, *Phys. Rev. B* **53**, 876 (1996).
11. H. F. Fong, B. Keimer, D. Reznik, D. M. Milius, I. A. Aksay, *Phys. Rev. B* **54**, 6708 (1996).
12. P. Bourges, in *The Gap Symmetry and Fluctuations in High Temperature Superconductors*, J. Bok *et al.*, Eds. (Plenum, New York, 1998), pp. 349–371 (e-Print available at http://xxx.lanl.gov/abs/cond-mat/9901333).
13. L. P. Regnault, P. Bourges, P. Burlet, in *Neutron Scattering in Layered Copper-Oxide Superconductors*, A. Furrer, Ed. (Kluwer, Amsterdam, 1998), pp. 85–134.
14. H. F. Fong, B. Keimer, F. Dogan, I. A. Aksay, *Phys. Rev. Lett.* **78**, 713 (1997).
15. P. Bourges *et al.*, *Europhys. Lett.* **38**, 313 (1997).
16. P. Dai *et al.*, *Phys. Rev. Lett.* **80**, 1738 (1998).
17. H. A. Mook *et al.*, *Nature* **395**, 580 (1998).
18. M. Arai *et al.*, *Phys. Rev. Lett.* **83**, 608 (1999).
19. D. van der Marel, *Phys. Rev. B* **51**, 1147 (1995).
20. F. Onufrieva and P. Pfeuty, e-Print available at http://xxx.lanl.gov/abs/cond-mat/9903097.
21. J. Brinckmann and P. Lee, *Phys. Rev. Lett.* **82**, 2915 (1999).
22. Y.-J. Kao, Q. Si, K. Levin, e-Print available at http://xxx.lanl.gov/abs/cond-mat/9908302.
23. K.-K. Voo and W. C. Wu, e-Print available at http://xxx.lanl.gov/abs/cond-mat/9911321.
24. H. F. Fong *et al.*, *Phys. Rev. B.*, in press (e-Print available at http://xxx.lanl.gov/abs/cond-mat/9910041).
25. On IN8, a Cu(111) monochromator and a pyrolytic graphite PG(002) analyzer, set at a fixed final energy of 35 meV, were used. On 2T, PG(002) was employed as both monochromator and analyzer with a 14.7-meV fixed final energy. In both experiments, a PG filter was inserted into the scattered beam to remove higher order contamination. The sample was wrapped in aluminum foil and attached to the cold finger of a closed-cycle helium refrigerator.
26. For simplicity, we describe the data with an isotropic dispersion relation (α independent of *q*). A slight anisotropy of α between the (100) and (110) directions, with an associated intensity modulation, would reproduce the detailed momentum dependence reported in (*17*).
27. Above 45 meV, the magnetic peaks are characterized by a broader response (*18, 24*) reminiscent of the spin waves of the undoped compound [see P. Bourges *et al.*, *Phys. Rev. B* **56**, R11439 (1997)].
28. A. V. Balatsky and P. Bourges, *Phys. Rev. Lett.* **82**, 5337 (1999).
29. P. Bourges *et al.*, in *High Temperature Superconductivity*, S. E. Bames *et al.*, Eds. (American Institute of Physics, Amsterdam, 1999), pp. 207–212 (e-Print available at http://xxx.lanl.gov/abs/cond-mat/9902067).
30. G. Aeppli, T. E. Mason, S. M. Hayden, H. A. Mook, J. Kulda, *Science* **278**, 1432 (1997).

31. We thank P. Baroni for his help during the experiment at Laboratoire Léon Brillouin and G. Aeppli, B. Hennion, G. Khaliullin, F. Onufrieva, and P. Pfeuty for stimulating discussions. The work at Princeton University was supported by the Materials Research Science and Engineering Centers program of the NSF under DMR-9809483.

17 January 2000; accepted 29 March 2000

Propagation of Seismic Ground Motion in the Kanto Basin, Japan

Kazuki Koketsu* and Masayuki Kikuchi

The pattern of ground motion for a magnitude 5.7 earthquake near Tokyo was captured by 384 strong ground motion instruments across the Kanto sedimentary basin and its surroundings. The records allow the visualization of the propagation of long-period ground motion in the basin and show the refraction of surface waves at the basin edge. The refracted wave does not travel directly from the earthquake epicenter, but traverses the basin obliquely to the edge. The surface wave inside the basin propagates more slowly than that outside such that the wavefronts separate from each other, and the refracted wave heals the discrepancy in the speed of advance of the wavefronts inside and outside the basin. The refracted arrival is dominant near the edge of the Kanto basin.

Seismic ground motion should be distorted and amplified by its propagation through sedimentary basins (*1*). However, observations of the effects of such propagation are limited because there have not been dense networks of strong ground motion seismometers that extend beyond the basins. Following the destructive earthquake in Kobe in 1995, the Japanese government realized that lack of prompt information on ground motion distribution was fatal to rescue and recovery actions immediately after a large earthquake. As a result, a dense network of strong ground motion seismometers and seismic intensity meters was installed across Japan (*2*, *3*). The intensity meters observe ground motion like a strong ground motion seismometer and automatically calculate the seismic intensity defined by the Japan Meteorological Agency.

Tokyo is situated in a large-scale sedimentary basin called the Kanto basin with an area of about 17,000 km^2. More than 600 strong ground motion instruments have been installed in the basin and its surroundings (Fig. 1). A magnitude 5.7 earthquake at a depth of 2.8 km on 3 May 1998 off the Izu peninsula (to the southwest of Tokyo) was observed by 384 sensors. This kind of shallow undersea earthquake often generates long-period surface Love waves, and these waves are clearly seen in the Kanto basin with periods of about 8 s (*4*). The large number of observations enabled us to visualize the propagation of the ground motion associated with these Love waves. To emphasize these arrivals, we first converted the accelerograms recorded by the instruments to velocity seismograms and applied a low-pass filter with a corner period of 5 s (Fig. 2A). Then we plotted the trajectories of ground motion in the horizontal plane for consecutive 10 s intervals after source initiation (Fig. 2, A to D) overlaid on an index map. These plots provide a clear indication of the progression of Love wave energy across the set of sensors.

The density of the instrument distribution, especially in the western mountain range, is not sufficient to allow interpolation of the data to produce a spatially continuous distribution of the ground motion. However, the Love wave generates ground motion parallel to its wavefront (perpendicular to its propagation path), so the trajectory of ground motion at each observation point can help us identify the wavefront and path. We normalized each particle trajectory to the maximum amplitude for the recording duration to make visible small ground motions in the mountain range (Fig. 2).

We identified wavefronts by noting abrupt changes in the amplitude and trajectory of ground motion. Small, near-circular motion before the arrival of the Love wave represents long-period components of the S body waves and is noticeable in the northeastern part of Fig. 2D due to the effects of the local geology. The pattern of particle motion in the center of the basin is contaminated by

Earthquake Research Institute, University of Tokyo, Tokyo 113-0032, Japan.

*To whom correspondence should be addressed. E-mail: inquiry@taro.eri.u-tokyo.ac.jp